International Journal of Nanoelectronics and Materials
Volume 15, No. 3, July 2022 [207-222]

Synthesis of MWCNTs/TiO_2 Photocatalytic Nanocomposite Membrane via *In-situ* Colloidal Precipitation Method for Methyl Orange Removal

Kah Chun Ho[1**], Sahira Mohammad Raffi[1], and Yeit Haan Teow[2]

[1]Centre for Water Research, Faculty of Engineering, Built Environment and Information Technology., SEGi University, Jalan Teknologi, Kota Damansara, 47810 Petaling Jaya, Selangor Darul Ehsan, Malaysia.
[2]Department of Chemical and Process Engineering, Faculty of Engineering and Built Environment, Universiti Kebangsaan Malaysia, 43600, UKM Bangi, Selangor Darul Ehsan, Malaysia.

Received 14 February 2022, Revised 18 February 2022, Accepted 6 April 2022

ABSTRACT

This research aims to examine the performance of photocatalytic nanocomposite membrane for methyl orange dye (MO) removal. Multiwalled carbon nanotubes (MWCNTs) and titanium dioxide (TiO_2) are used as nanofillers to produce photocatalytic membranes via in-situ colloidal precipitation method. The weight ratio of MWCNT:TiO_2 were manipulated at 10:0, 5:5, and 0:10 with nanomaterials concentration of 0.1 g/L. The membranes were characterized by surface hydrophilicity, porosity and pore size, and surface charge. The membrane performance was assessed using dead-end membrane filtration method to determine water permeability, dye rejection, and fouling propensity. Pure TiO_2 membrane improved water permeability by 22.57% due to increasing hydrophilicity and large porosity. For dye rejection, pristine membrane outperformed the nanocomposite membranes with a rejection of 25.52% due to the small membrane pore size by sieve mechanism. Lastly, all the nanocomposite membranes showed better antifouling properties with higher normalized flux for pure MWCNTs (0.6822), TiO_2 (0.6781), MWCNT/TiO_2 (0.7239) membranes relative to the pristine membrane (0.6039). The pure TiO_2 membrane has the highest improvement in flux recovery (19.87%) due to dye photodegradation under UV light assisted in membrane cleaning and defouling. Overall, this study demonstrates that photocatalytic nanocomposite membrane can be produced via in-situ colloidal precipitation method.

Keywords: *In-situ* colloidal precipitation method, Multiwalled carbon nanotubes, Nanocomposite membrane, Titanium dioxide

1. INTRODUCTION

Wastewaters containing dyes are unsafe for humans, aquatic life, and microorganisms. These dyes and chemical compounds break down and pollute the soil, sediments, and surface waters consequently posing a major global environmental danger [1]. Therefore, dye wastewater must be treated according to the legal guidelines to protect the environment. Membrane processes are special technology for wastewater treatment that has many benefits, including high efficiency, ease to use, no phase changes, high selectivity, and minimal energy utilization [2, 3]. Nevertheless, the membrane fouling restricts membrane-wide applications because of foulant adhesion and flux deterioration [4, 5].

Recently, it has been reported that photocatalytic membranes can effectively minimize membrane fouling [6]. As UV or visible light reaches the photocatalytic membrane, the photocatalyst generated hydroxyl radicals (•OH) that oxidize the organic foulant into carbon dioxide and water. This reduces the adhesion of foulant, hence recovering the water flux. Nanomaterials like titanium dioxide (TiO_2) have shown great potential as photocatalyst to

*Corresponding author: hokahchun@segi.edu.my

produce photocatalytic membranes. TiO_2 is the most photoactive material because of its capacity for oxidizing, chemical strength, and low cost; but TiO_2 has not achieved the anticipated photocatalytic behavior due to wide band gaps (3.0–3.2 eV between phases) [7]. Theoretically, the efficiency of photoinduced electron transfer of TiO_2 can be enhanced by pairing it with a good electron acceptor. Multiwalled carbon nanotubes (MWCNTs) are excellent electron acceptors that can receive electrons by light irradiation. Then, the electrons can transport to the conduction band of TiO_2, thus improving the rate of photocatalysis reactions [8]. However, the main problem of using nanomaterials in membrane fabrication is aggregation. High nanomaterial concentrations may cause nanomaterial aggregation and membrane defects [7].

In-situ colloidal precipitation is instantaneous membrane pore formation and nanomaterials incorporation in the coagulation bath. Meng et al. [9] reported that graphene oxide (GO) in coagulation bath (5-20 mg/L) has decreased the contact angle of the synthesized membranes indicated improved hydrophilicity due to the attachment of hydrophilic GO onto the membranes. Similarly, Zhang et al. [10] reported that the increase of carbon nanosphere (CNS) concentration from 0 mg/L to 400 mg/L has decreased contact angle and increased negatively-charged potential of membranes, suggesting a strong potential for membrane modification. These studies proved that *in-situ* colloidal precipitation method has managed to produce nanocomposite membrane with uniformly distributed nanomaterials to enhance membrane performance without the compensation of membrane characteristics. Nevertheless, to the best of our knowledge, MWCNTs/TiO_2 has not been investigated as hybrid nanofillers to synthesize photocatalytic nanocomposite membrane via *in-situ* colloidal precipitation method.

The objective of this study is to fabricate MWCNTs/TiO_2 photocatalytic nanocomposite membranes and study the effect of nanomaterial ratio (MWCNTs:TiO_2) on membrane performance. The membrane properties including hydrophilicity of the surface, porosity, and pore size were characterized. Synthetic methyl orange (MO) dye was used to investigate the membrane performance during the dead-end membrane filtration system.

2. MATERIAL AND METHODS

2.1 Materials

TiO_2 purity of ≥99.5% with a nanoparticle size of 21 nm was obtained from Sigma Aldrich, Malaysia. MWCNTs purity of >97% with length of 3-15 μm and diameter of 12-15 nm were obtained from Ugent Tech, Malaysia. Dimethylacetamide (DMAc) (grade of ≥99%) supplied by Merck Co., Germany was used to dissolve polyvinylidene fluoride (PVDF) (PVDF T-1) supplied by Shanghai Ofluorine. MO was purchased from Evergreen Engineering and Resources, Malaysia.

2.2 Membrane Synthesis

Membrane synthesis via *in-situ* colloidal precipitation method is divided into three stages: coagulation bath preparation, polymer solution synthesis, and membrane casting. The coagulation bath was prepared using various MWCNT:TiO_2 weight ratios (10:0, 5:5, and 0:10) at concentration of 0.1 g/L. MWCNTs/TiO_2 were added to RO water and sonicated using ultrasonicator (Avantor Inc., USA) for 30 minutes to improve nanomaterial stability in a coagulation bath. Then, PVDF powder was dissolved in DMAc and agitated at 250 rpm for 4 hours at 65°C using a magnetic stirrer. Then, it was agitated for another 4 hours at 40°C at 250 rpm [11]. PVDF: DMAc membrane polymer solution was fixed at 15:85 (wt%) [12]. The membrane polymer solution was left idle 24 hours to degas. Lastly, approximately 25 mL of the membrane polymer solution was poured on membrane support (CU414 Opti, Neenah US). The motorized film applicator and bar coater were used to cast a 200 μm thin film with thickness at a speed of 7 cm/s

[13]. Then, the thin film was submerged directly into the prepared coagulation bath. The membrane was held for one day to guarantee phase inversion [14]. Table 1 shows the formulation of membrane polymer solution and coagulation bath.

Table 1 Membrane polymer solution and coagulation bath formulation

Membrane abbreviation	Nanomaterials ratio (g/g)		Concentration of nanomaterials in bath (g/L)
	MWCNTs	TiO_2	
M1a	0	0	0
M1b	10	0	0.1
M1c	5	5	0.1
M1d	0	10	0.1

2.3 Membrane Characteristics

2.3.1 Surface Hydrophilicity

Surface hydrophilicity was determined using an Attention Theta contact angle goniometer (Biolin Scientific, Sweden). A high-speed camera system was installed at a contact angle goniometer. The water droplet fell onto the membrane surface and images were automatically taken. The captured image was studied using OneAttension software to calculate the contact angle.

2.3.2 Porosity and Pore size

A gravimetrical approach based on water sorption was employed to calculate the volume of liquid occupied in membrane pores [15]. The pre-soaked membrane was then chopped into tiny pieces (1 cm × 1 cm). Membrane thickness was measured using a micro thickness gauge. The porosity of the membrane was measured with Equation 1 [16]:

$$\mathcal{E} = \frac{\frac{W_1 - W_2}{\rho_W}}{\frac{W_1 - W_2}{\rho_W} + \frac{W_2}{\rho_P}} \times 100\% \quad (1)$$

where, ε is the membrane porosity, (%), W_1 is the wet weight of the membrane, (g), W_2 is the dry weight of the membrane, (g), ρ_W is the density of distilled water, 0.998 g/mL, ρ_P is the density of the polymer, PVDF = 1.765 g/mL at 25°C [17].

Guerout-Elford-Ferry based on filtration velocity was used to calculate the mean pore size of the membrane as shown in Equation 2 [18]:

$$r_m = \sqrt{\frac{(2.9 - 1.75\mathcal{E})8\eta IQ}{\mathcal{E} \times A \times \Delta P}} \quad (2)$$

where, r_m is the membrane mean pore radius, (m), ε is the membrane porosity, (%), η is the water viscosity, 8.9×10^{-4} Pa s, l is the membrane thickness, (m), Q is the permeate volume per unit time, (m^3/s), A is the membrane area, (m^2) and ΔP is the operational pressure, (Pa).

2.3.3 Surface Charge

The membrane surface charge was determined by the Zeta Sizer, Nano-ZS (Malvern Instruments Inc., UK). The membrane sample was mounted on zeta potential cell, ZEN 1020 (Malvern Instruments Inc., UK), and immersed in saline solution containing latex with particle size of 300–350 nm. The mobility of latex particles at various distances from the membrane sample was used to assess the charge on the membrane surfaces.

2.4 Performance Evaluation of Membrane

2.4.1 Membrane Permeability Test

Performance of membranes synthesized using *in-situ* colloidal precipitation method was evaluated using a dead-end membrane filtration system. Figure 1 shows the dead-end membrane filtration system consisting of ultrafiltration cell Millipore 8050 (Merck, Germany) [19].

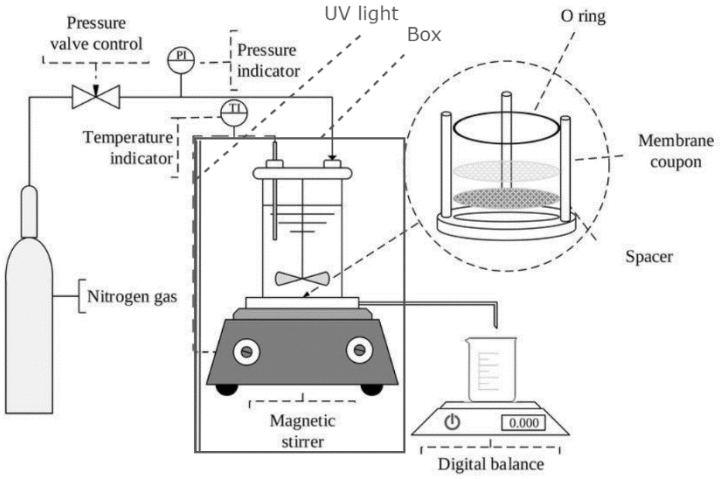

Figure 1. Dead-end membrane filtration setup [19]

Prior to the membrane permeability test, the membrane was compacted with a steady 3 bar pressure for 20 minutes to minimize compaction effects. During the permeability test, RO water at various trans-membrane pressure (TMP) of 0.5,1.0, and 1.5 bar was applied. Membrane flux was calculated by permeate volume obtained over the permeation period using Equation 3 [20]:

$$J = \frac{\Delta V}{A \Delta t} \tag{3}$$

where, J is the permeate flux, (L/m^2 h), ΔV is the permeate volume, (L), A is the effective membrane filtration area, (m^2) and Δt is the permeation time, (h).

2.4.2 Dye Rejection Test

In the rejection experiment, 30 mg/L MO was used as feed. The membrane was tested for 25 minutes at 1 bar. Rejection of MO was measured at a 5-minute interval and determined using Equation 4 [21]:

$$R = \left[1 - \frac{C_P}{C_f}\right] \times 100\% \tag{4}$$

where, R is the membrane rejection, (%), C_P is the concentration of permeate, (mg/L) and C_f is the concentration of feed solution, (mg/L).

2.4.3 Membrane Antifouling Test

A similar setup in Figure 1 was used to test membrane antifouling characteristics. The distance between the membrane surface and the UV light SLV/25 15W UV-C light (Philips, Malaysia) is 45 cm. At this distance, a thermometer's reading of light heating might be ignored [22]. The dead-end cell was initially filled with 30 mg/L MO, and membrane filtration was operated for 30 minutes at 1 bar. Then, the UV light was powered on for 5 minutes to start the photocatalysis process every 5-minute interval. The process was repeated for 3 cycles. Membrane antifouling properties were defined as normalized flux calculated by Equation 5:

$$Normalized\ Flux = \frac{J_1}{J} \tag{5}$$

where, J_1 is the permeate flow system with MO dye as feed solution for membrane filtration, and J is the pure water flux.

3. RESULTS AND DISCUSSION

3.1 Membrane Synthesis

Figure 2 shows the optical images of the synthesized membrane via *in-situ* colloidal precipitation method. As shown, the pristine membrane (M1a) was observed to be colorless while the pure MWCNTs membrane (M1b) appeared black and pure TiO_2 membrane (M1d) appeared white. This is because the physical appearance of MWCNTs and TiO_2 nanomaterials are black and white, respectively [23]. Meanwhile, the MWCNTs/TiO_2 membrane (M1c) shows a lighter color than the pure MWCNTs membrane (M1b). From observation during the *in-situ* colloidal precipitation process, the DMAc solvent diffused out from the membrane polymer solution while the nanomaterials and water moved into the membrane matrix. Figure 3 shows the schematic diagram of membrane formation via *in-situ* colloidal precipitation method. This process induced the instantaneous membrane pore formation and nanomaterials incorporation without altering the membrane structure significantly [24].

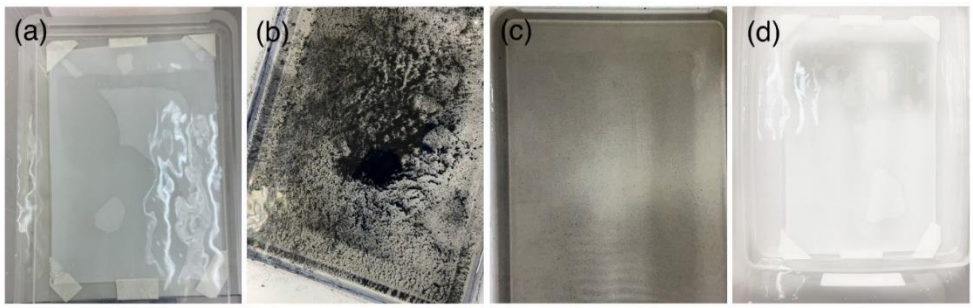

Figure 2. Optical images for: (a) M1a, (b) M1b, (c) M1c, and (d) M1d membranes synthesized via i*n-situ* colloidal precipitation

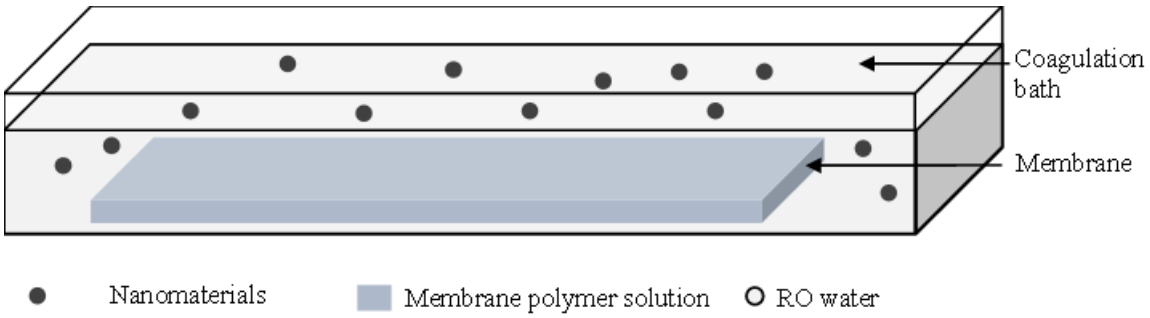

Figure 3. Schematic diagram of membrane formation via in-situ colloidal precipitation method

3.2 Membrane Characteristics

3.2.1 Surface Hydrophilicity

Table 2 indicates the contact angle of membranes measured in 3 separated spots of the membrane. As seen, the contact angle of the pristine membrane (M1a) is 59.46°. The incorporation of pure MWCNTs and TiO_2 to membranes has increased the contact angle to 76.17° (M1b) and 71.11° (M1d). This is due to the development of water droplets between nanomaterials and the surface of membranes as evidenced by images of water droplets on M1a and M1b (Figure 4). Unlike the conventional direct blending method, the nanomaterials tend to adhere on the membrane surface during the *in-situ* colloidal precipitation, increasing the membrane roughness. Nevertheless, it should be emphasized that the contact angle measurement is influenced by membrane surface hydrophilicity and other membrane surface properties such as functional groups, zeta potential, and surface roughness [25]. Studies have reported that a membrane surface that is chemically hydrophobic will become even more hydrophobic when surface roughness is increased [26].

Table 2 Contact angle of membranes

Membrane Abbreviation	Contact Angle (°)			
	1st Trial	2nd Trial	3rd Trial	Average
M1a	57.13	61.79	59.46	59.46 ± 1.90
M1b	73.50	77.32	77.69	76.17 ± 1.89
M1c	44.00	46.01	46.65	45.55 ± 1.13
M1d	73.50	71.63	68.19	71.11 ± 2.20

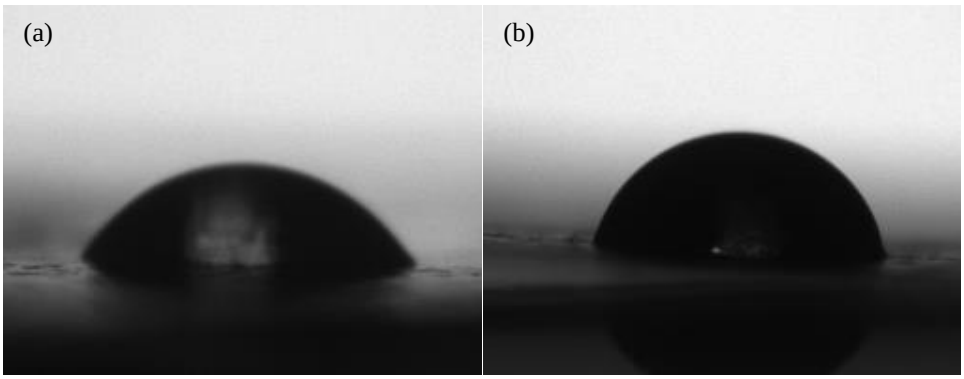

Figure 4. Images of water droplets on (a) M1a and (b) M1b membranes

For MWCNTs/TiO_2 membrane (M1c), the contact angle decreases from 59.46° (M1a) to 45.55° (M1c) signifying that the membrane has higher hydrophilicity. Unlike the pure MWCNTs (M1b) and TiO_2 (M1d) membrane, the incorporation of MWCNTs/TiO_2 in weight ratio of 5:5 has helped the uniform dispersion of TiO_2 on the MWCNTs surface and implying a strong interphase structure effect between TiO_2 and MWCNTs [27]. MWCNTs and TiO_2 formed strong interphase structure by carbonyl group coordination and ester bonding between carboxyl group of MWCNTs and TiO_2. Hence, the mixture of MWCNTs/TiO_2 nanomaterials incorporated evenly on the membrane surface during the *in-situ* colloidal precipitation and formed a smoother surface. This resulted in the M1c membrane wet spontaneously with water and reduced contact angle.

3.2.2 Porosity and Pore Size

Table 3 shows the porosity and mean pore size radius of the membrane. In general, the porosity of the synthesized membranes improved with the incorporation of nanomaterials on the membrane surface. This is because of the incorporation of MWCNTs and TiO_2 nanomaterials increasing solvent outflux and water influx thermodynamics in solution equilibrium hence forming a more porous membrane [28]. Besides, it is worth to note that TiO_2 increased membrane porosity (56.18 %) more than that of MWCNTs (44.11 %) when they are added to the membranes. This is because MWCNTs did increase the viscosity of the coagulation bath and result in a decrease in mutual diffusion rate hence lower porosity increment compared to TiO_2 [29].

In terms of pore size, the incorporation of MWCNTs and MWCNTs/TiO_2 reduced the membrane's pore size (M1b, M1c). This is because of the structures of long and fibrous MWCNTs (length <10 μm) being capable of blocking the membrane pore, leading to the reduction of pore size. Whereas, the irregularly shaped TiO_2 size of 21 nm could be located inside some of the pore walls, hence water is still capable of passing through the membrane easily. This is also in agreement with the findings by Esfahani et al. [30], where their research prepared nanocomposite membranes using varying ratios of TiO_2 and MWCNTs at fixed concentration constant of 1 wt%. They reported that the membrane pore size was dominated by MWCNTs effects relative to TiO_2.

Table 3 Porosity and mean pore radius of membranes

Membrane Abbreviation	Porosity, ε (%)	Mean pore radius r_m (nm)
M1a	40.60±15.25	748.09±74.66
M1b	44.11±11.35	688.00±73.28
M1c	49.30±10.51	674.87±11.65
M1d	56.18±14.58	819.72±63.52

3.2.3 Surface Charge

Figure 5 shows the surface charge of membrane determined by zeta potential. The zeta potential of the pristine membrane (M1a) is slightly negatively charged (-8.30 mV). This is because of adsorption of counter anions such as chloride and hydroxyl ions onto hydrophobic PVDF membrane surfaces [31]. The incorporation of nanomaterials (MWCNTs and TiO_2) increased the zeta potential of synthesized membranes to -0.78 mV (M1b), +1.61 mV (M1c), and +5.39 mV (M1d). This is because both MWCNTs and TiO_2 possess positive charges of +13.87 mV and +0.61 mV, respectively [32][33]. Hence, the incorporation of these nanomaterials neutralizes the negativity of anions adsorbed on membrane surface and subsequently increases the positivity of the membrane. As the MO dye is anionic azo dye (negatively charged), it is expected that the MO dye will be more readily attracted by the positively charged membrane surface (M1c and M1d) and affecting membrane rejection and fouling propensity.

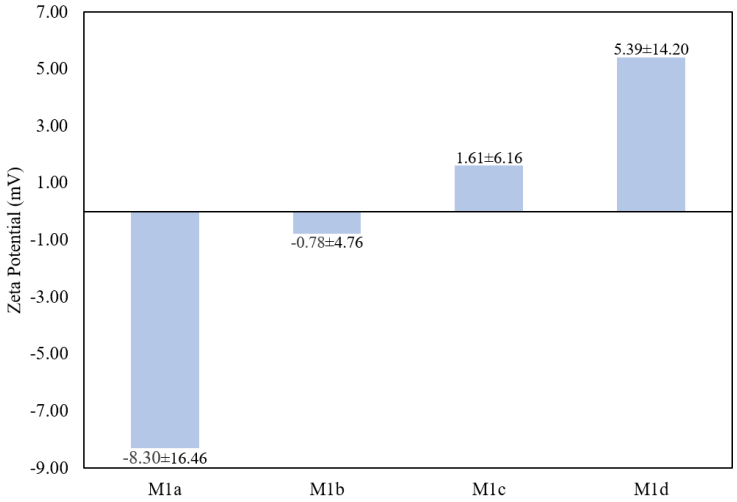

Figure 5. Zeta potential of membranes

3.3 Membrane Performance

3.3.1 Membrane Permeability Test

Figure 6 shows the water permeability of the synthesized membranes. As shown, the pristine membrane (M1a) has a water permeability of 48.33 L/m^2.h.bar. The incorporation of MWCNTs and MWCNTs/TiO_2 decreased the water permeability of the membranes to 41.45 L/m^2.h.bar (M1b) and 43.82 L/m^2.h.bar (M1c), respectively. This is supported by the membrane pore size presented in Table 3. The M1b and M1c membranes have smaller pore size (674.87-688 nm) compared to the M1a membrane (748 nm), hence, water has a higher resistance to permeate through the membrane resulting in lower water permeability. Besides, it is worth noting that the impact of pore size of the membranes on membrane permeability is more significant compared to hydrophilicity at the surface [34]. It is reported that 50 % of the solvent flow is through 20-25 % of the membrane pores for ultrafiltration process [35]. Whereas, the pure TiO_2 membrane (M1d) has a higher water permeability (59.23 L/m^2.h.bar) than the pristine membrane (M1a). This is owing to the higher porosity and pore size of the nanocomposite membrane that allows faster permeation of water as shown in Table 3. However, having larger pore sizes results in a lower separation factor which may affect the membrane rejection.

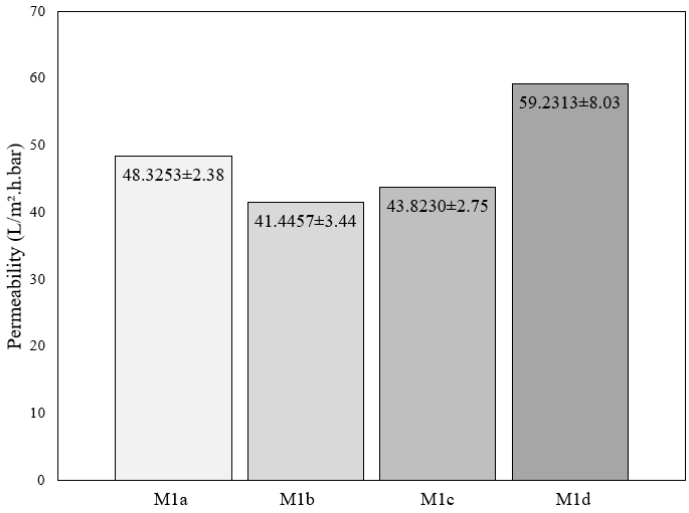

Figure 6. Permeability of membranes

3.3.2 Membrane Rejection Using Dye

Table 4 shows the dye rejection of membranes measured at 5-minute interval of membrane filtration. A comparatively low rejection performance was realized for the membranes in this study. This is attributed to the low molecular weight of MO dye and large pore size of synthesized membranes. The molecular diameter of MO dye is approximately 6-8 nm while the pore radius of the synthesized membrane is 674.87-819.72 nm [36]. Hence, the MO dye passes through the membrane pore freely and resulted in low rejection.

For the first cycle, the pristine membrane (M1a) shows the highest rejection (25.52%) of MO compared to other nanocomposite membranes (10.36-16.97%). This is justified by electrostatic repulsion by the surface charge of the membranes and dye. As the MO dye is anionic azo dye (negatively charged), it will be repelled from the membranes that have a more negatively charged surface. As illustrated in Figure 5, the zeta potential of pristine membrane (M1a) is the lowest (-8.30 mV), hence the repulsion of negatively-charged MO dye from the negatively-charged membrane is the highest. This resulted in the highest rejection of dye in the pristine membrane (M1a). The pure TiO_2 membrane (M1d) has the lowest rejection (10.36%) of MO amongst all the synthesized membranes. This is because the M1d has the largest pore size (819.72 nm) and the highest zeta potential (+5.39 mV), hence the MO dye is ready to diffuse into the pores and the membrane surface, decreasing the rejection values [37]. The concentration of MO in the permeate obtained using M1d ranges from 26.89-29.39 mg/L.

Table 4 Membrane rejection

Cycle	Time (min)	Rejection (%)			
		M1a	**M1b**	**M1c**	**M1d**
First cycle	**5**	25.5208	11.1292	16.9677	10.3586
	10	UV Cleaning			
Second cycle	**15**	11.5501	6.0561	7.3948	6.8317
	20	UV Cleaning			
Third cycle	**25**	6.1598	1.4226	5.1225	2.0451

After 5 minute of membrane filtration, the membranes were exposed to UV light to initial the photocatalysis for 5-minute duration. It can be observed from Table 4 that the rejection of dye

has decreased for all the synthesized membranes. As the membrane filtration proceeds, the MO dye forms a thicker cake layer on the membrane surface resulting in cake-enhanced concentration polarization. The accrued dye solutes at the membrane surface increase the concentration gradient across the membrane resulting in rise of permeate concentration and thus, a reduction in dye rejection. This result is also consistent with Yangali-Quintanilla et al. [38]. They found that NF-200 membrane fouling with sodium alginate worsened the performance of the membrane. Thus, membrane fouling affects the rejection of hydrophilic neutral compounds and hydrophilic and hydrophobic ionic compounds. This is because of the restricted back diffusion of compounds to the bulk solution and resulting transport across the membrane.

Besides, it is observed that membrane UV cleaning helps to retain the rejection of MO dye in certain membranes. Despite the rejection of dye decreased after UV cleaning, the decrease of the MO dye rejection is the lowest for pure TiO_2 membrane, M1d (34.05%) and MWCNTs/TiO_2 membrane, M1c (30.73%) compared to pristine membrane, M1a (54.74%) and pure MWCNTs membrane, M1b (76.51%). As shown in Table 4, the dye rejection performance of M1d merely decreased by 34.05% from 10.36% to 6.83% while the dye rejection performance of M1a decreased significantly by 54.74% from 25.52% to 11.55%. This can be explained by the synergism of photocatalysis and filtration by UV light under the presence of TiO_2 photocatalyst. The catalytically active edges of TiO_2 triggered the photocatalytic synthesis of radicals that attach to the MO dye, subsequently achieving mineralization [39].

3.3.3 Membrane Antifouling Using UV Light

Figure 7 shows the membrane antifouling properties represented by normalized flux as a function of time. In general, MWCNTs/TiO_2 photocatalytic nanocomposite membranes have better antifouling properties with higher normalized flux values of 0.6822 (M1b), 0.6781 (M1c), and 0.7239 (M1d) compared to the pristine membrane, M1a (0.6039) after 25 minutes. This is mainly attributed to the membrane surface charge.

For the first cycle, the pure MWCNTs (M1b) membrane displayed the best antifouling properties indicated by the highest normalized flux (0.91). This can be explained by the surface charge of the M1b membrane. As revealed by Figure 5, the zeta potential of M1b membrane is -0.78 mV, hence more of the negatively-charged MO dye will be repelled from the negatively charged M1b membrane surface. Despite the M1a membrane having a lower zeta potential of -8.30 mV, the water permeability of the M1a membrane is higher, forming a thicker cake layer on the membrane caused by the high permeation drag [40]. Owing to high permeation drag, partial of the MO dye overcame an energy barrier before they contacted the membrane surface, hence causing higher fouling propensity. On the contrary, the MWCNTs/TiO_2 (M1c) membrane has a surface charge of +1.61 mV, hence the negatively charged MO dye is more readily adsorbed to the positively charged membrane surface and causes severe membrane fouling.

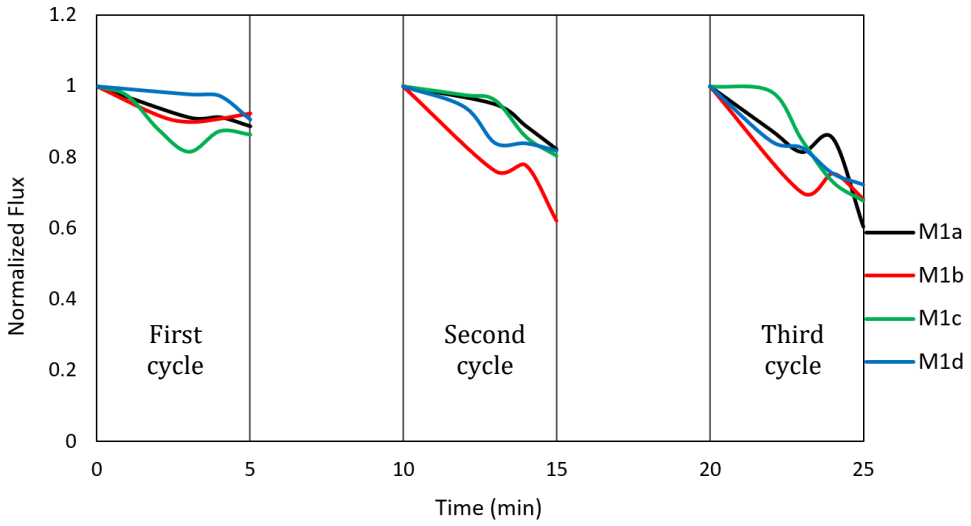

Figure 7. Normalized flux of membranes as a function of time

After 5 minute of membrane filtration, the membranes were exposed to UV light to initialize the photocatalysis for 5-minute duration. As seen from Figure 7, the pure TiO_2 (M1d) membrane displayed the best antifouling properties indicated by the highest normalized flux in the second cycle (0.82) and third cycle (0.72). This can be best explained by the photodegradation of dye by UV light under the presence of TiO_2 photocatalyst. The produced free radicals generated by photoexcited electron-hole pairs on TiO_2 photocatalyst are responsible for breaking the MO organic compounds that stubbornly adhered inside the pores and on the membrane surface. This reduced the cake layer formed by MO dye, hence recovered the initial membrane flux. As mentioned, the molecular size of MO is significantly smaller than membrane pore size; it is expected that the photodegradation of dye could occur on the membrane surface and within the pores. As the photodegradation proceeds, the oxidized byproduct of MO dye includes carbon dioxide and water could pass through the membrane easily [41]. As compared to MWCNTs/TiO_2 membranes (M1c), the M1c membrane cannot attain the expected normalized flux. This could be due to the interaction of TiO_2 nanoparticles with MWCNTs which change the process of e^--h^+ formation by inducing charge transfer behavior and enhance photocatalytic properties of TiO_2 under visible light irradiation [42]. Hence, the UVC irradiation provided in this experiment may not able to trigger the photocatalytic activity of MWCNTs. This is in agreement with study by Krissanasaeranee et al. [43] that CNTs could decompose contaminants under UV–Vis light.

4. CONCLUSION

In conclusion, this study has successfully developed novel photocatalytic nanocomposite membrane using MWCNTs and TiO_2 as nanofillers via *in-situ* colloidal precipitation method. The incorporation of nanomaterials like MWCNTs and TiO_2 has significantly impacted the membrane characteristics. The incorporation of MWCNTs and TiO_2 increases solvent outflux and water influx thermodynamics in solution equilibrium, hence forming a more porous membrane. For pore size, the incorporation of MWCNTs and MWCNTs/TiO_2 reduced the pore size of the membranes because of the long and fibrous MWCNTs blocking the membrane pore. In terms of membrane performance in MO dye removal, the pure TiO_2 (M1d) membrane displayed the best antifouling properties indicated by the highest normalized flux in the second cycle (0.82) and third cycle (0.72). This is because of the photodegradation of dye by UV light under the presence of TiO_2 photocatalyst. The produced free radicals generated by TiO_2 photocatalysts are responsible for breaking the MO organic compounds that stubbornly adhered on the membrane surface and inside the pores. Unfortunately, MWCNTs fail to attain the expected antifouling properties.

Further research should investigate the wavelength of UV-vis light for attaining outstanding photocatalysis and filtration for dye wastewater treatment.

ACKNOWLEDGEMENTS

This research is fully supported by SEGi Internal Research Fund grant, SEGiIRF/2022-Q1/FoEBEIT/002. The authors fully acknowledged Department of Chemical and Process Engineering of UKM for laboratory analysis.

REFERENCES

[1] Yaseen, D.A., & M. Scholz, "Textile dye wastewater characteristics and constituents of synthetic effluents: a critical review", International Journal of Environmental Science and Technology. **16** (2019) 1193–1226.
[2] Chen, W., J. Mo, X. Du, Z. Zhang, & W. Zhang, "Biomimetic dynamic membrane for aquatic dye removal", Water Research. **151** (2019) 243–251.
[3] Meng, S., X. Meng, W. Fan, et al., "The role of transparent exopolymer particles (TEP) in membrane fouling: A critical review", Water Research. **181** (2020).
[4] Li, R., H. Fan, L. Shen, et al., "Inkjet printing assisted fabrication of polyphenol-based coating membranes for oil/water separation", Chemosphere. **250** (2020).
[5] Rao, L., J. Tang, S. Hu, et al., "Inkjet printing assisted electroless Ni plating to fabricate nickel coated polypropylene membrane with improved performance", Journal of Colloid and Interface Science. **565** (2020) 546–554.
[6] Nasrollahi, N., L. Ghalamchi, V. Vatanpour, & A. Khataee, "Photocatalytic-membrane technology: a critical review for membrane fouling mitigation", Journal of Industrial and Engineering Chemistry. **93** (2021) 101–116.
[7] Etacheri, V., C. Di Valentin, J. Schneider, D. Bahnemann, & S.C. Pillai, "Visible-light activation of TiO2 photocatalysts: Advances in theory and experiments", Journal of Photochemistry and Photobiology C: Photochemistry Reviews. **25** (2015) 1–29.
[8] Chen, M.L., & W.C. Oh, "Synthesis and highly visible-induced photocatalytic activity of CNT-CdSe composite for methylene blue solution", Nanoscale Research Letters. **6** (2011) 1–8.
[9] Meng, N., Z. Wang, Z.X. Low, Y. Zhang, H. Wang, & X. Zhang, "Impact of trace graphene oxide in coagulation bath on morphology and performance of polysulfone ultrafiltration membrane", Separation and Purification Technology. **147** (2015) 364–371.
[10] Zhang, J., Z. Wang, M. Liu, F. Zhao, & Z. Wu, "In-situ modification of PVDF membrane during phase-inversion process using carbon nanosphere sol as coagulation bath for enhancing anti-fouling ability", Journal of Membrane Science. **526** (2017) 272–280.
[11] Ngang, H.P., B.S. Ooi, A.L. Ahmad, & S.O. Lai, "Preparation of PVDF-TiO2 mixed-matrix membrane and its evaluation on dye adsorption and UV-cleaning properties", Chemical Engineering Journal. **197** (2012) 359–367.
[12] Ho, K.C., Y.H. Teow, A.W. Mohammad, W.L. Ang, & P.H. Lee, "Development of graphene oxide (GO)/multi-walled carbon nanotubes (MWCNTs) nanocomposite conductive membranes for electrically enhanced fouling mitigation", Journal of Membrane Science. **552** (2018) 189–201.
[13] Ooi, C.S., & M.K. Chan, "Nano Iron Oxide Impregnated Poly(Vinylidene Fluoride) Ultrafiltration Membrane for Palm Oil Mill Effluent Treatment", Journal of Engineering & Technological Advances. **4** (2019) 11–23.
[14] Zhang, Y., & T.S. Chung, "Graphene oxide membranes for nanofiltration", Current Opinion in Chemical Engineering. **16** (2017) 9–15.
[15] Ayyaru, S., & Y.H. Ahn, "Application of sulfonic acid group functionalized graphene oxide to improve hydrophilicity, permeability, and antifouling of PVDF nanocomposite ultrafiltration membranes", Journal of Membrane Science. **525** (2017) 210–219.
[16] Rezaee, R., S. Nasseri, A.H. Mahvi, et al., "Fabrication and characterization of a polysulfone-graphene oxide nanocomposite membrane for arsenate rejection from water", Journal of Environmental Health Science and Engineering. **13** (2015) 61.

[17] Zhao, C., X. Xu, J. Chen, & F. Yang, "Optimization of preparation conditions of poly(vinylidene fluoride)/graphene oxide microfiltration membranes by the Taguchi experimental design", Desalination. **334** (2014) 17–22.
[18] Xu, Z., J. Zhang, M. Shan, et al., "Organosilane-functionalized graphene oxide for enhanced antifouling and mechanical properties of polyvinylidene fluoride ultrafiltration membranes", Journal of Membrane Science. **458** (2014) 1–13.
[19] Starr, B.J., V. V. Tarabara, M. Zhou, S. Roualdès, & A. Ayral, "Coating porous membranes with a photocatalyst: Comparison of LbL self-assembly and plasma-enhanced CVD techniques", Journal of Membrane Science. **514** (2016) 340–349.
[20] Yuliwati, E., A.F. Ismail, T. Matsuura, M.A. Kassim, & M.S. Abdullah, "Characterization of surface-modified porous PVDF hollow fibers for refinery wastewater treatment using microscopic observation", Desalination. **283** (2011) 206–213.
[21] Chan, M.K., & M. Letchumanan, "Improved Hydrophilicity of Membrane by Ethylenediaminetetraacetic Acid Modification", Journal of Applied Membrane Science & Technology. **23** (2018).
[22] Yeit Haan Teow, Boon Seng Ooi, Abdul Latif Ahmad, & Jit Kang Lim, "Investigation of Anti-fouling and UV-Cleaning Properties of PVDF/TiO2 Mixed-Matrix Membrane for Humic Acid Removal", Membranes. **11** (2021) 16.
[23] Zetty Akhtar, A.M., M.M. Rahman, K. Kadirgama, S. Rahman, & M.A. Maleque, "Thermal Conductivity and Viscosity of TiO2/MWCNTs (doped 10wt% graphene) - Ethylene Glycol Based Nanofluids for Different Ratio of Nanoparticle", Journal of Advanced Research in Fluid Mechanics and Thermal Sciences. **72** (2020) 32–46.
[24] Teow, Y.H., A.L. Ahmad, J.K. Lim, & B.S. Ooi, "Preparation and characterization of PVDF/TiO2mixed matrix membrane via in situ colloidal precipitation method", Desalination. **295** (2012) 61–69.
[25] Ho, K.C., Y.H. Teow, W.L. Ang, & A.W. Mohammad, "Novel GO/OMWCNTs mixed-matrix membrane with enhanced antifouling property for palm oil mill effluent treatment", Separation and Purification Technology. **177** (2017) 337–349.
[26] Attension TN 7, "Influence of surface roughness on contact angle and wettability", Www.Attension.Com. (2015) 1–3.
[27] El-Sayed, B.A., W.A.A. Mohamed, H.R. Galal, H.M. Abd El-Bary, & M.A.M. Ahmed, "Photocatalytic study of some synthesized MWCNTs/TiO2 nanocomposites used in the treatment of industrial hazard materials", Egyptian Journal of Petroleum. **28** (2019) 247–252.
[28] Lee, J., H.R. Chae, Y.J. Won, et al., "Graphene oxide nanoplatelets composite membrane with hydrophilic and antifouling properties for wastewater treatment", Journal of Membrane Science. **448** (2013) 223–230.
[29] Koutahzadeh, N., M.R. Esfahani, & P.E. Arce, "Sequential use of UV/H2O2-(PSF/TiO2/MWCNT) mixed matrix membranes for dye removal in water purification: Membrane permeation, fouling, rejection, and decolorization", Environmental Engineering Science. **33** (2016) 430–440.
[30] Esfahani, M.R., J.L. Tyler, H.A. Stretz, & M.J.M. Wells, "Effects of a dual nanofiller, nano-TiO2 and MWCNT, for polysulfone-based nanocomposite membranes for water purification", Desalination. **372** (2015) 47–56.
[31] Kakihana, Y., L. Cheng, L.F. Fang, et al., "Preparation of positively charged PVDF membranes with improved antibacterial activity by blending modification: Effect of change in membrane surface material properties", Colloids and Surfaces A: Physicochemical and Engineering Aspects. **533** (2017) 133–139.
[32] Halimi, S.U., N.F. Abu Bakar, S.N. Ismail, S.A. Hashib, & M.N. Naim, "Electrospray deposition of titanium dioxide (TiO2) nanoparticles", AIP Conference Proceedings. **1586** (2014) 57–62.
[33] Tserengombo, B., H. Jeong, E. Dolgor, A. Delgado, & S. Kim, "Effects of functionalization in different conditions and ball milling on the dispersion and thermal and electrical conductivity of mwcnts in aqueous solution", Nanomaterials. **11** (2021).
[34] Hassan, M.L., S.M. Fadel, R.E. Abouzeid, et al., "Water purification ultrafiltration membranes using nanofibers from unbleached and bleached rice straw", Scientific Reports. **10** (2020).
[35] Fane, A.G., C.J.D. Fell, & A.G. Waters, "The relationship between membrane surface pore characteristics and flux for ultrafiltration membranes", Journal of Membrane Science. **9** (1981) 245–262.
[36] Wu, L., X. Liu, G. Lv, et al., "Study on the adsorption properties of methyl orange by natural one-dimensional nano-mineral materials with different structures", Scientific Reports. **11** (2021).
[37] Heu, R., M. Ateia, & C. Yoshimura, "Photocatalytic nanofiltration membrane using Zr-MOF/GO nanocomposite with high-flux and anti-fouling properties", Catalysts. **10** (2020).
[38] Yangali-Quintanilla, V., A. Sadmani, M. McConville, M. Kennedy, & G. Amy, "Rejection of pharmaceutically active compounds and endocrine disrupting compounds by clean and fouled nanofiltration membranes", Water Research. **43** (2009) 2349–2362.

[39] Rameshkumar, S., R. Henderson, & R.B. Padamati, "Improved surface functional and photocatalytic properties of hybrid zno-mos2-deposited membrane for photocatalysis-assisted dye filtration", Membranes. **10** (2020).
[40] Teow, Y.H., Y.H. Chiah, K.C. Ho, & E. Mahmoudi, "Treatment of semiconductor-industry wastewater with the application of ceramic membrane and polymeric membrane", Journal of Cleaner Production. **337** (2022).
[41] Leong, S., A. Razmjou, K. Wang, K. Hapgood, X. Zhang, & H. Wang, "TiO2 based photocatalytic membranes: A review", Journal of Membrane Science. **472** (2014) 167–184.
[42] Song, C., P. Chen, C. Wang, & L. Zhu, "Photodegradation of perfluorooctanoic acid by synthesized TiO2-MWCNT composites under 365nm UV irradiation", Chemosphere. **86** (2012) 853–859.
[43] Krissanasaeranee, M., S. Wongkasemjit, A.K. Cheetham, & D. Eder, "Complex carbon nanotube-inorganic hybrid materials as next-generation photocatalysts", Chemical Physics Letters. **496** (2010) 133–138.
[44] Dai, K., X. Zhang, K. Fan, P. Zeng, & T. Peng, "Multiwalled carbon nanotube-TiO2 nanocomposite for visible-light-induced photocatalytic hydrogen evolution", Journal of Nanomaterials. **2014** (2014).